NANO LETTERS
Letter
Cite This: Nano Lett. 2019, 19, 5229−5236
pubs.acs.org/NanoLett

# In Situ Electrochemical Mapping of Lithium−Sulfur Battery Interfaces Using AFM−SECM

Kiran Mahankali, Naresh Kumar Thangavel, and Leela Mohana Reddy Arava*

Department of Mechanical Engineering, Wayne State University, 5050 Anthony Wayne Drive, Detroit, Michigan 48202, United States

Supporting Information

**ABSTRACT:** Although lithium−sulfur (Li−S) batteries are explored extensively, several features of the lithium polysulfides (LiPS) redox mechanism at the electrode/electrolyte interface still remain unclear. Though various in situ and ex situ characterization techniques have been deployed in recent years, many spatial aspects related to the local electrochemical phenomena of the Li-S electrode are not elucidated. Herein, we introduce the atomic-force-microscopy-based scanning electrochemical microscopy (AFM−SECM) technique to study the Li−S interfacial redox reactions at nanoscale spatial resolution in real time. In situ electrochemical and alternating current (AC) phase mappings of $Li_2S$ particle during oxidation directly distinguished the presence of both conducting and insulating regions within itself. During charging, the conducting part undergoes dissolution, whereas the insulating part, predominantly $Li_2S$, chemically/electrochemically reacts with intermediate LiPS. At higher oxidation potentials, as-reacted LiPS turns into insulating products, which accumulate over cycling, resulting in reduction of active material utilization and ultimately leading to capacity fade. The interdependence of the topography and electrochemical oxidative behavior of $Li_2S$ on the carbon surface by AFM−SECM reveals the $Li_2S$ morphology−activity relationship and provides new insights into the capacity fading mechanism in Li−S batteries.

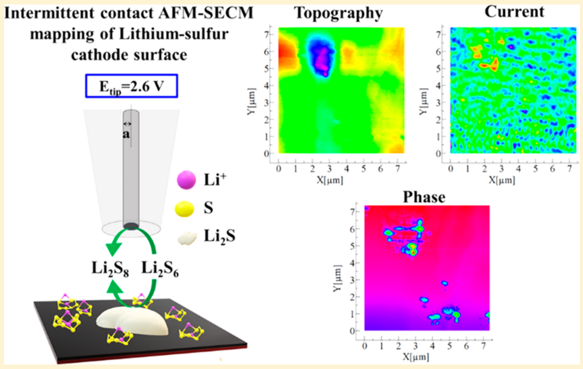

**KEYWORDS:** *Scanning electrochemical microscopy, lithium−sulfur, in situ, electrochemical mapping, topography, $Li_2S$ oxidation*

Although lithium−sulfur (Li−S) batteries hold significant promise as the next-generation technology to replace lithium-ion batteries, their development is still hampered by several challenges such as rapid capacity fade, short cycle life, and poor Coulombic efficiency.[1−3] The primary reason behind these performance barriers is the dissolution of lithium polysulfides (LiPS) , their subsequent parasitic reactions (i.e., "polysulfide shuttle effect"). and electronically insulating solid discharge end product formation at the cathode surface.[4−6] The polysulfide shuttle effect was evaded by accelerating the conversion of the liquid LiPS into solid product deposits ($Li_2S_2$/$Li_2S$).[7−9] However, the inherent insulating nature of such deposits decreases the electrochemically active area and increases the cell resistance, resulting in overpotential and capacity fade issues over prolonged cycling.[10−15] To address these issues, extensive research efforts were devoted to finding better electrode and electrolyte materials. However, only a limited emphasis was given toward understanding the true nature of polysulfide interactions at the electrode/electrolyte interface, mainly because of the nonexistence of a comprehensive tool to grasp the working mechanism in real time. Although much of the in situ studies envisage the nature of LiPS reactivity along with their chemical identity in different electrolytes,[16−19] a detailed temporal and spatial mapping of LiPS interactions on the electrode surface has not been explored much.[20,21] Nevertheless, some techniques such as X-ray diffraction (XRD),[1,22] transmission electron microscopy (TEM),[23] and transmission X-ray microscopy (TXM)[24] have successfully revealed the significance of the morphology of $Li_2S$ (the solid end product of discharge) in determining the reversible capacity and rate capability of the Li−S cells.

Recently, the electrochemically irreversible nature of $Li_2S_2$ was elucidated using in situ atomic force microscopy (AFM) coupled with ex situ Raman and X-ray photoelectron spectroscopy (XPS) characterization of the LiPS/electrode interface at nanoscale spatial resolution.[25] Further, at micrometer resolution, in situ X-ray fluorescence microscopy (XRF) identified incomplete oxidation of $Li_2S$ during the charging process and proposed that the particle size was dependent on it.[26] In addition, the same study has revealed the morphological changes associated with the redistribution of sulfur/polysulfides and identified the growth of electrochemically inactive sites over cycling. Though these studies provide a certain level of understanding of the topographical influence on

**Received:** April 19, 2019
**Revised:** July 16, 2019
**Published:** July 19, 2019

DOI: 10.1021/acs.nanolett.9b01636

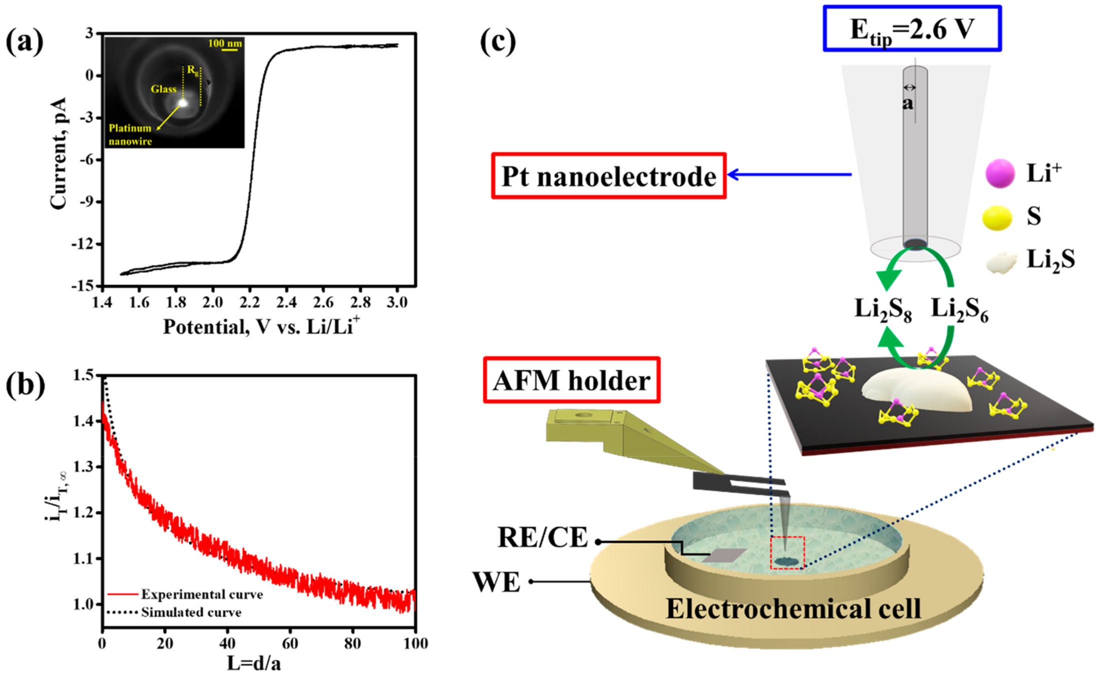

**Figure 1.** AFM−SECM Pt tip performance: (a) cyclic voltammogram of cobaltocene redox mediator on AFM−SECM Pt tip (diameter = 100 nm), far away from the substrate ($i_{T,\infty}$), SEM image of the Pt tip (inset); (b) steady state approach curve. Tip biased at reduction potential of 2.1 V, and substrate biased at oxidation potential of 2.4 V. Tip Approach performed using a stepper motor at a speed of 0.0003 $\mu$m/msec. (c) Schematic representation of SECM electrochemical cell setup (details given in Supporting Information) and zoom-in part depicts the competitive SECM mode used for imaging of Li-S cathode surface where the substrate was biased between 2.5 to 2.7 V, and tip was biased at a constant potential of 2.6 V vs Li/Li$^+$.

Li−S charge/discharge reactions, they fall short on providing electrochemical perspectives of the interfacial reactions. On the other hand, scanning electrochemical microscopy (SECM) techniques that involve probing an electrochemical surface with ultramicroelectrodes (UMEs) provides information about the reaction kinetics and topography at micro/nanoscale levels with high temporal and spatial resolutions, respectively.[27,28] Previously, SECM was utilized for exploring the morphological changes and mapping the localized redox activity/hotspots of active material in Li-ion batteries.[29−31] However, SECM was never deployed in investigating the redox reactions of the Li−S system, mainly because of the fact that the sulfur cathode undergoes phase transformations during charge/discharge processes, and probing such a dynamic system is complicated. However, successful implementation of SECM in the Li−S system will unprecedently provide newer insights, for example, regarding the origin of electrochemical inactive regions, which is expected to shed light on several issues occurring at the Li−S cathode surfaces.

In this manuscript, for the first time, we have employed atomic-force-microscopy-based scanning electrochemical microscopy (AFM−SECM) to study the Li−S cathode surface at a nanoscale spatial resolution in real time. Herein, with the help of competitive SECM mode current mapping, we have chosen to study the interdependence of $Li_2S$ morphology on its electrochemical activity during oxidation. The implementation of this SECM imaging technique was first evidenced with a typical electrode surface in a LiPS environment while maintaining appropriate experimental conditions and then utilized to study the $Li_2S$ oxidation in realistic conditions. The observed findings were further corroborated by in situ AFM topography and in situ Raman experiments as given in detail.

Initially, AFM−SECM platinum (Pt) nanoelectrodes commercially purchased from Nanonics Imaging Ltd. were mounted onto an AFM scanner head (cell assembly details given in Supporting Information (SI)) and were used for the entirety of the studies. Figure 1a, inset, shows the SEM image of the Pt tip used in this study. The Pt tip has a conical shape with a diameter of 100 nm and an $R_g$ factor (ratio of glass sheath to tip) of 2. Unlike traditional SECM (tip-current-based positioning), integrated nanoelectrodes with an AFM probe with a certain oscillation amplitude control the tip−substrate distance independently from the electrochemical signal. Thus, these nanoelectrodes enable a concurrent measurement of the local electrochemical activity and topographical changes, which are complementary to each other. Prior to the feedback measurements to infer the tip−substrate distance, the tip performance was evaluated by cyclic voltammetry (Figure 1a) with a cobaltocene redox mediator dissolved in nonaqueous solvents (substrate performance is shown in Figure S1). The tip voltammogram showed a well-defined sigmoidal shape with negligible capacitive current, indicating the suitability of the Pt tip for electrochemical mapping.

The steady state current of the $Co^{2+}/Co^{3+}$ redox mediator recorded at the Pt tip far away from the substrate ($i_{T,\infty}$) was found to be 13 pA, and the diffusion coefficient for the cobaltocene redox mediator was determined to be $3.3 \times 10^{-6}$ cm$^2$/sec (the detailed calculation is provided in the SI). Next, in the SECM-feedback mode, the tip and the substrate were biased at $Co^{3+}/Co^{2+}$ reduction and oxidation potentials, respectively, to record the tip current ($i_T$) vs distance ($d$) at a preset tip approach speed of 0.0003 $\mu$m/ms. The tip current was found to gradually increase with tip translation toward the substrate, which indicates positive feedback approach at the Pt tip (Figure 1b). The experimental curve fits the positive feedback theoretical curve until $L = 3.85$, and the tip-to-substrate distance was found to be 193 nm (details of the approach curve measurement and curve fitting are given in the SI). The $L$ value obtained here is appropriate to maintain $d/a \gg 1$ to avoid problems due to interference by the diffusion layers between the substrate and the tip, and is suitable for various SECM operating modes like generation-collection and competition.[32] In addition, the unique feature to control the function of the SECM tip using alternating current (AC) frequency oscillation can inherently provide phase shift images complementary to the topography and electrochemical images. It is believed that these images can provide multidimensional information regarding the dynamics of the surface.

Herein, for SECM imaging of the Li−S cathode surface, more specifically during $Li_2S/Li_2S_2$ oxidation, we have employed the competitive SECM mode[33−35] (as shown in Figure 1c) which is a variation of generation-collection mode. In this approach, both the tip and substrate compete for the same electrochemically active intermediate LiPS under oxidative conditions. When scanning in an $x,y$-plane over the surface at a constant distance, the LiPS oxidation current remains constant as long as the SECM tip is on a normal surface. However, if the tip crosses the diffusion zone of LiPS on a highly active area on the electrode surface, the local LiPS concentration within the tip−substrate gap gets decreased, thereby causing a reduced tip current.

Preceding the experiment, to identify the appropriate oxidation potentials for SECM mapping, the voltammetric response was recorded on the SECM Pt tip and carbon surface in $Li_2S_6$ polysulfide solution between 3.0 to 1.8 V vs $Li/Li^+$. The voltammetric response recorded on the carbon surface, as shown in Figure S2a, displayed two cathodic peaks at 2.40 and 2.00 V vs $Li/Li^+$, corresponding to the conversion of long-chain LiPS to short-chain LiPS and their subsequent conversion to discharge end products, respectively. During the reverse sweep, a broad anodic peak at potentials >2.55 vs $Li/Li^+$ was observed, which can be ascribed to the $Li_2S$ oxidation process. The observed Li−S redox potential, with the SECM cell setup, was found to be slightly shifted as compared to the typical potential plateaus seen in coin-cell configurations. The shift in redox potential can be anticipated when potentiodynamic conditions are employed, where currents and ohmic drops continuously change but remain constant under galvanostatic experiments.[36,37] For this reason, the shift in the redox peak potentials was often witnessed in several three-electrode systems[38,39] and in situ characterization studies that are aimed at probing redox interfaces in Li−S[25] and other Li-ion batteries.[30] Further, as shown in the tip voltammogram (Figure S2b), the SECM electrode displayed typical sigmoidal waves at appropriate potentials of $Li_2S_6$ reduction and oxidation reactions. It has been elucidated that the oxidation of $Li_2S$ produces $Li_2S_6$, the only stable and predominant electroactive intermediate LiPS, in the first step. The as-formed $Li_2S_6$ undergoes further electrochemical oxidation to $S_8^{2-}$ at higher potentials, finally leading to the formation of $S_8$.[40,41] As the $Li_2S_6$ is the only electroactive species present before the formation of solid inactive $S_8$, we made an effort to use this species to establish the competition mode necessary for imaging. On the basis of the above-mentioned observations, a potential of 2.6 V was chosen as $E_{tip}$, and the substrate potential was biased between 2.4 to 2.8 V for SECM mapping of $Li_2S$ oxidation. In addition, the characteristic small capacitive current (Figure S2b) is low in comparison to the Faradaic current, which indicates that the electron transfer conversion reactions of LiPS are facilitated at the UME. This would not have been possible if solid products deposit during reduction and remain on the electrode surface, where one could see an increase in capacitive current in the oxidation side. Hence, fouling of the Pt nanoelectrode surface because of the sulfur reaction and its interferences on the tip performance are not expected in this study.

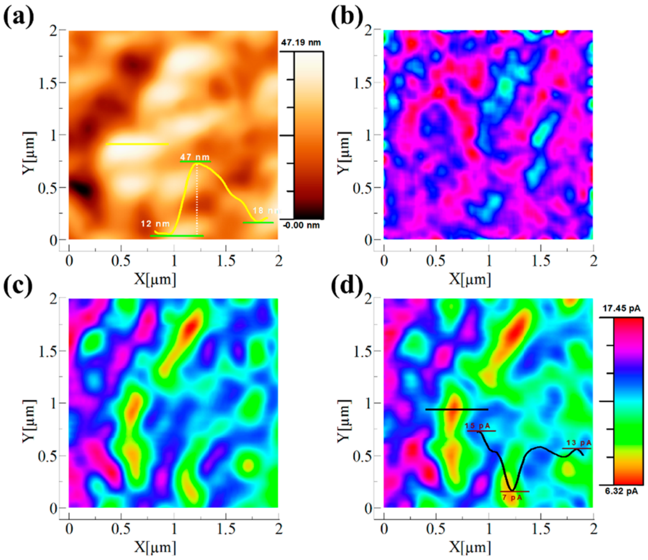

**Figure 2.** Competitive SECM mode in $Li_2S_6$ solution: (a) AFM−height image of electrochemically deposited platinum nanoparticles on carbon (inset: height profile of a particle). SECM current images recorded by biasing the tip at 2.6 V and the substrate at (b) 2.5, (c) 2.6, and (d) 2.7 V vs $Li/Li^+$ (inset; current distribution on the particles).

To prove the compatibility of $Li_2S_6$ as a redox mediator for SECM competitive mode, we performed a control experiment using a Pt nanoparticle modified carbon surface, in $Li_2S_6$ solution. Figure 2a shows the AFM topography image (scan area of 2 × 2 $\mu$m) of electrodeposited Pt nanoparticles, on a carbon surface, with an average particle height of about 24 nm. Initially, the tip current was recorded by biasing the Pt tip at 2.6 V, which corresponds to the oxidation potential of $Li_2S_6$, at a constant distance. Next, the substrate was biased at different potentials between 2.5−2.7 V vs $Li/Li^+$, as shown in Figures 2b−d, and AFM−SECM line scanning was performed across the $x,y$-plane. At 2.5 V, the substrate did not show any activity, and the tip current was uniform throughout the surface, indicating no oxidation process. On the other hand, when the substrate's potential was tuned to a higher potential of 2.6 V, decreased tip currents were observed when the tip crosses a Pt nanoparticle compared to the other areas of the surface. Such behavior is certainly due to the establishment of the competition mode at 2.6 V, where $Li_2S_6$ oxidation is predominant on the Pt surface, thus depleting its availability at the tip, thereby decreasing the tip current. Similar trends were observed when the substrate was biased at 2.7 V, with even further decrease in tip currents indicating more reactivity of the Pt surface rather than the Pt tip. These results are in good agreement with phase contrast images, as shown in Figure S3, which indicate a change in-phase values from (−) to (+) at the Pt particle at these potential regions. The presented results demonstrate the feasibilty of employing the competitive

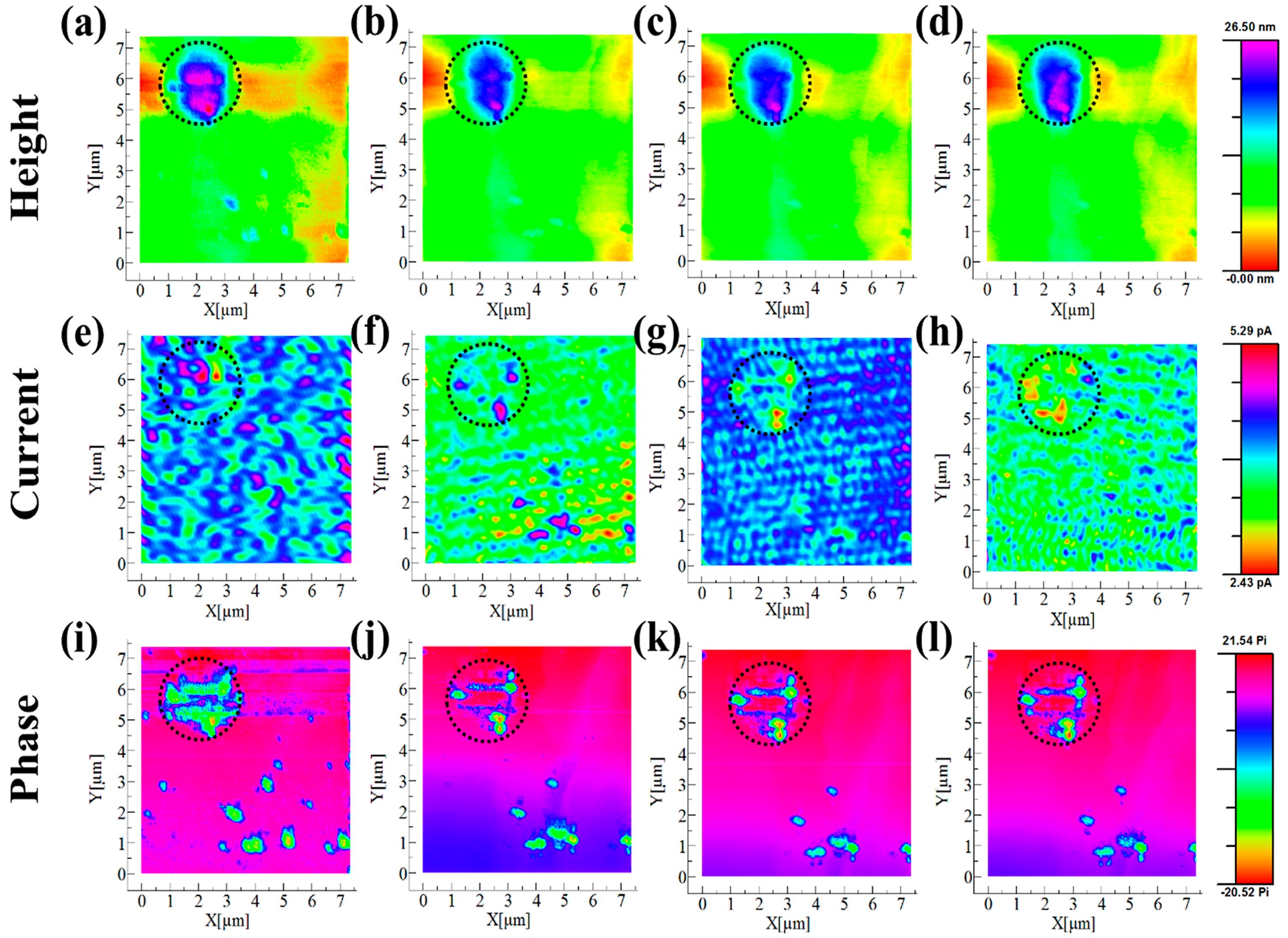

**Figure 3.** AFM−SECM imaging of $Li_2S/Li_2S_2$ on carbon surface during oxidation: simultaneous height (first row), current (second row), and phase shift (third row) mapping of $Li_2S/Li_2S_2$ surface. First column images (a,e,i) correspond to $Li_2S/Li_2S_2$ [galvanostatically deposited] on glassy carbon before oxidation; second, third, and fourth column images correspond to the $Li_2S$ oxidation at different substrate potentials of 2.5 (b,f,j), 2.6 (c,g,k), and 2.7 V (d,h,l) vs $Li/Li^+$ respectively; $E_{tip}$ = 2.6 V.

SECM mode for electrochemical mapping of the Li−S cathode surface with intermdiate LiPS ($Li_2S_6$) as a redox mediator.

After the validation of SECM competition mode in ideal conditions, we now applied it to practical Li−S system by choosing the oxidation reaction of discharge end products ($Li_2S/Li_2S_2$). Initially to ensure $Li_2S/Li_2S_2$ deposition, the LiPS reduction process was subjected to typical nucleation (galvanostatic discharge from open circuit potential to 2.05 V vs $Li/Li^+$) followed by a growth process.[42] The SECM study was performed under the following conditions: (i) after $Li_2S/Li_2S_2$ growth, excess LiPS was replaced with blank electrolyte to suppress the simultaneous side reactions of liquid LiPS (details provided in SI), and (ii) to simplify the SECM imaging and to avoid the influence of a neighboring particle's reactivity on tip current, we have performed line scanning selectively on a single $Li_2S/Li_2S_2$ particle with the help of AFM software, as shown in Figure 3a. The data is presented here after the experiments were replicated twice to validate the obtained results. Prior to the line scan, a constant potential of 2.6 V was applied to the substrate for 15 min; to generate $Li_2S_6$, at the same time, the tip was kept far away from the surface. Next, the Pt tip approached the surface using the AFM feedback mode and was positioned at a constant distance. Figure 3b−d, f−h, and j−l depict the simultaneously recorded height, current, and phase images on the $Li_2S/Li_2S_2$ particle, respectively, at different oxidation potentials between 2.5 to 2.7 V vs $Li/Li^+$; meanwhile, the tip was kept at a constant potential of 2.6 V.

At 2.5 V, a decrease in the height and volume of the particle was observed, which can be ascribed to the oxidation of $Li_2S/Li_2S_2$ to $Li_2S_6$. However, a higher tip current was observed on the particle at this potential, an observation similar to the control experiment. Interestingly, the height of the $Li_2S/Li_2S_2$ particles was found to increase at 2.6 V and further increased at 2.7 V, indicating particle growth at higher oxidation potentials. Simultaneously, current mapping at 2.6 V reveals that the tip current started to decline on the particle, which further depleted at 2.7 V (as depicted by the black circles in Figure 3g,h), whereas currents on other areas of the substrate remains unchanged. Noticeably, changes in the tip current were observed only on certain regions, whereas the current profile on other areas of the particle matches with the substrate, which indicates an inhomogeneity in the composition of the $Li_2S/Li_2S_2$ particle. The decrease in tip current is independent of the changes in tip−sample distance, and the observed tip features indicate the occurrence of some intriguing surface phenomenon within the $Li_2S/Li_2S_2$ particle. To gain further insights into the tip current heterogeneity on the $Li_2S/Li_2S_2$ particle, AC phase contrast images were analyzed. It is denoted for the AC phase shift that the positive and negative signs correspond to the in-phase and out-of-phase, respectively, which can be

DOI: 10.1021/acs.nanolett.9b01636
Nano Lett. 2019, 19, 5229−5236

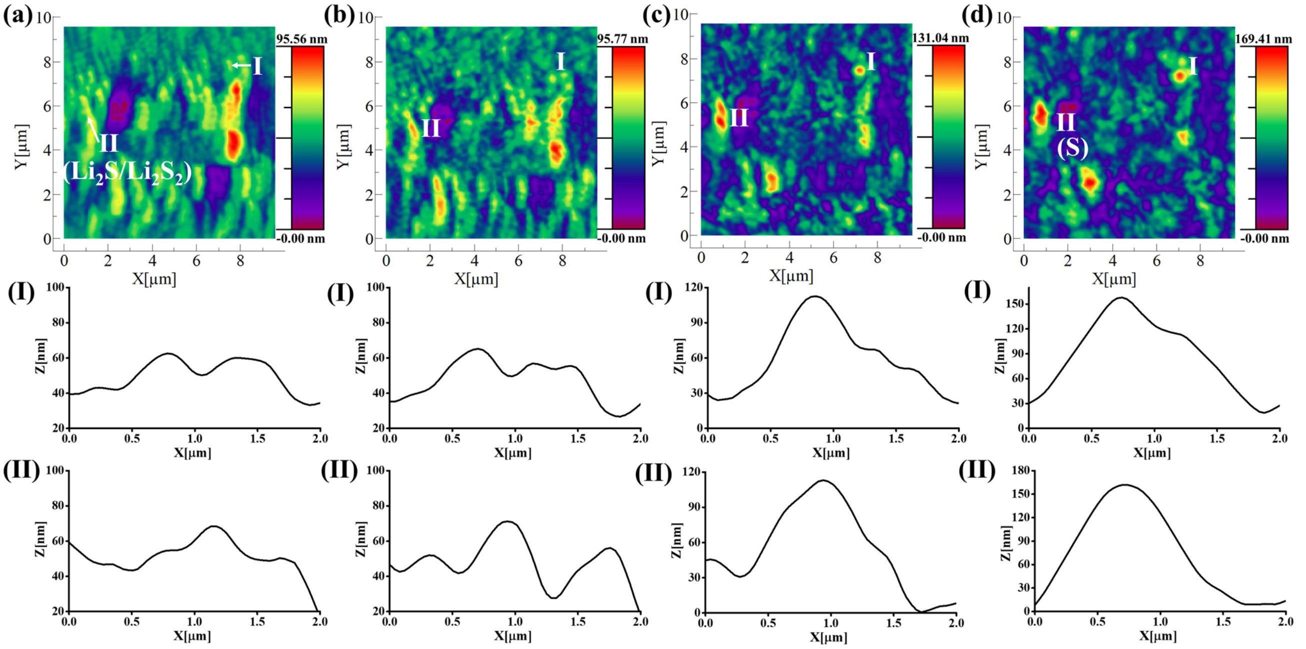

**Figure 4.** In situ AFM mapping of Li−S cathode surface: (a) images of $Li_2S/Li_2S_2$ [galvanostatically deposited] on glassy carbon before oxidation; $Li_2S/Li_2S_2$ oxidation at different potentials: (b) 2.5, (c) 2.6, and (d) 2.7 V vs $Li/Li^+$, respectively. [Scan area = 10 × 10 $\mu$m.] The line profiles of particles identified as I and II show height changes at corresponding potentials.

correlated to the conductive and insulating natures of the surface.[43] As shown in Figure 3i−l, the phase images show negative $\pi$ radians where tip currents get reduced as evidenced from bright contrast (green-orange colors) on the particle, whereas the remaining areas of the particle and carbon surfaces show similar phase contrast colors with positive $\pi$ radians. These phase contrast image reveals the existence of both conducting and insulating parts in the scanned particle. Several theoretical analyses elucidate that both $Li_2S_2$ and $Li_2S$ solid product forms at the end of discharge, and the former one is more electronically conductive than the later.[44−46] To identify possible discharge products, we have performed ex situ XPS and found that both $Li_2S$ and $Li_2S_2$ exists on the carbon surface (as shown in Figure S4, details provided in SI), which is agreed upon well by previous reports.[25,47,48] Given these facts and with present validation by the phase images, conducting and insulating parts of the particle can correspond to $Li_2S_2$ and $Li_2S$, respectively, which evidently addresses the inhomogeneity in the electrochemical reactivity of the particle.

Thus, while at charging potentials, the conducting regions of $Li_2S_2$ undergo oxidation readily, yielding intermediate LiPS, and the insulating part of $Li_2S$, which is electrochemically irreversible, remains on the surface. It has been previously elucidated that $Li_2S$ is chemically active in nature and exhibits strong adsorption energy toward intermediate polysulfides.[49] Hence, at potentials >2.6 V, the observed tip current changes can be directly correlated to the consumption of the as-formed $Li_2S_6$ (produced during oxidation) by the $Li_2S$ particle, depleting their concentration at the tip−substrate gap and thereby causing a decrease in tip current. As-adsorbed LiPS undergoes a chemical/electrochemical reaction with $Li_2S$ and forms electrochemically inactive particles as evidenced from the increased height of the particles and insulting area in the phase images. The changes in the particle height were further evidenced by the plot between the volume of the single particle and average particle height with respect to the applied potential (Figure S5). It is evident that the average height and volume of the particle decreased rapidly from 22.5 to 16 nm and 0.14 to 0.09 $\mu m^3$, respectively, when the potential was increased from 1.9 to 2.5 V. Further, even though a slight increase in particle height was noted at 2.6 V, as clearly depicted by the plot, no changes in volume was observed. Then, fast growth in both volume (up to 0.13 $\mu m^3$) and average particle height (up to 22 nm) were observed, further supporting the particle growth phenomenon occurring on the insulating particle at higher oxidative potentials. Previous reports have proposed the possible $Li_2S$ charging mechanism in conventional Li−S cells as follows: higher order polysulfides produced from short-chain polysulfide's oxidation undergo chemical/electrochemical reaction with $Li_2S$ until their complete conversion.[41] The obtained AFM−SECM results are in good agreement with the above prediction and provide direct visualization of such a reaction for the first time by current mappings with supporting evidence from AFM height and phase images.

Overall, with AFM−SECM images, we elucidate the following aspects by analyzing the single $Li_2S/Li_2S_2$ particles: (i) the Li−S discharge product consists of both $Li_2S_2$ and $Li_2S$, which are bound to each other; (ii) $Li_2S_2$ undergoes the oxidation reaction readily compared to the $Li_2S$; (iii) intermediate LiPS chemically/electrochemically reacts with $Li_2S$ with increasing potentials, which paves a way for insulating solid product deposition. Further, an increase in the height of the particle and a drastic decrease in the tip current on the particle were seen even at the oxidation potential of 2.8 V (Figure S6), where the conversion of $Li_2S_x$ ($x$ = 6−8, liquid state) to solid sulfur is eminent.[26,50] In addition, the phase contrast image at 2.8 V (Figure S6c) shows an increased contrast at the center of the particle, confirming the formation of rather insulating sulfur species at high oxidative potentials. To corroborate the observation that sulfur formation occurs even before the complete conversion of $Li_2S$

during the oxidation process, we have performed Raman measurement on that particle, which is shown in Figure S7. At the initial stage (2.4 V), the Raman spectrum shows a band at 376 $cm^{-1}$, which corresponds to the $Li_2S$.[51,52] The Raman intensity of the $Li_2S$ peak linearly reduced with increasing oxidative potential, which is due to the oxidation of $Li_2S$ to intermediate polysulfides ($Li_2S_6$, as indicated by the growth of the Raman band at 426 $cm^{-1}$).[53] Whereas, an additional Raman band at 468 $cm^{-1}$ (corresponding to solid sulfur[16]) started to grow from 2.6 V, and its intensity was found to increase linearly with increasing oxidative potentials, at the expense of $Li_2S_6$. The fact that the peak at 468 $cm^{-1}$ emerged even before the $Li_2S$ peak disappeared indicates the simultaneous existence of both $Li_2S$ and sulfur, which validates the results observed in AFM−SECM images. It is noteworthy to mention that in situ Raman observation of $Li_2S_6$ species during the oxidation process further corroborates that it is the only stable electroactive intermediate LiPS present before the formation of $S_8$ rather than any other short-lived intermediate LiPS. In short, the current in situ SECM study reveals the interdependence of topography and the electrochemical oxidative behavior of $Li_2S/Li_2S_2$ on the carbon surface, addressing the $Li_2S$ morphology−activity relationship.

Given the dependency of $Li_2S$ oxidation on its particle size[26] and to extrapolate the results observed on the single particle, we governed topographical changes of differently sized $Li_2S/Li_2S_2$ particles during oxidation, with in situ AFM as shown in Figure 4a−d. Initially to ensure $Li_2S/Li_2S_2$ deposition, the LiPS reduction process was subjected to typical nucleation (galvanostatic discharge from open circuit potential to 2.05 V vs $Li/Li^+$) followed by the growth process (potentiostatic treatment at different potentials). During the initial growth stage, at 2.0 V vs $Li/Li^+$, scattered deposition of $Li_2S/Li_2S_2$ particles was observed throughout the scan area ($10 \times 10$ μm, Figure S8). Further, with decreasing potentials until 1.9 V vs $Li/Li^+$, the particle growth was observed to be nonuniform with a height distribution in the range of 35 to 95 nm (Figure 4a). During oxidation, when a potential of 2.5 V was applied (Figure 4b), several smaller particles (below 50 nm) shrunk, indicating $Li_2S/Li_2S_2$ oxidation. However, at higher potentials (from 2.6 to 2.7 V, Figure 4c,d), commencement of the bigger $Li_2S/Li_2S_2$ particle's area shrinkage along with a further decrease in the density of smaller particles was noted. Similar to the single particle's behavior, we identified that some of the $Li_2S/Li_2S_2$ particle's (identified as I and II in Figure 4a−d) height increased (as given in line profile) with increasing oxidation potential. For instance, at 2.5 V, the height of one such particle (I) was found to be 65 nm, which was observed to increase to 120 and 150 nm at 2.6 and 2.7 V, respectively, indicating the growth of that particle. The increment in particle height is further corroborated by the histogram plot (Figure S9), which clearly shows the occurrence of new events at 2.7 V.

This in situ AFM study reveals an early oxidation of smaller particles compared to relatively bigger particles, which demonstrates a size-dependent oxidation process. Previously, several reports demonstrated that the morphology, composition, and physiochemical characteristics of the discharge products ($Li_2S/Li_2S_2$) can be closely correlated to the deteriorating performance issues like internal resistance buildup and capacity fade in Li−S cells.[10,12] On the basis of the AFM−SECM mapping of a single $Li_2S/Li_2S_2$ particle and the presented in situ AFM observations, it is safe to conclude that the smaller particles are $Li_2S_2$, and the bigger particles constitute both $Li_2S_2$ and $Li_2S$. During charging, smaller $Li_2S_2$ nanoparticles oxidize at initial stages, whereas the $Li_2S_2$ bound to the $Li_2S$ surface gets oxidized at higher overpotentials. However, unoxidized $Li_2S$ particles chemically/electrochemically react with the intermediate LiPS (produced during $Li_2S_2$ oxidation) and encourage electronically inactive particle formation at higher oxidation potentials as evidenced from the particle's height increment on certain regions. Such accumulation of inactive particles over insulating $Li_2S$ partially blocks further oxidation of $Li_2S$, whereas inactive particles are deprived of their electronic conduction path for subsequent reduction. Thus, consecutive deposition of charge and discharge active materials (on bigger $Li_2S$ particles) on the carbon surface unequivocally limits both oxidation and reduction processes in a Li−S system over cycling. Ultimately, this process is known to increase the internal resistance of the cell and loss of active material, thereby leading to a rapid capacity fade. Further to validate the in situ AFM−SECM results in more realistic conditions, we have performed a typical galvanostatic charge/discharge experiment with liquid LiPS in a controlled manner. Figure S10 shows the AFM height profile of changes observed during $Li_2S/Li_2S_2$ precipitation and its oxidation under discharge/charge conditions (at a rate of 20 $\mu A/cm^2$) in two different potential regions. As expected, with increasing depth of discharge, the height of deposited $Li_2S/Li_2S_2$ particles increased, and particles of wide size ranges were observed, Figure S10a,b. However, at initial stages of charging, the height of those particles decreased as shown in Figure S10c, which indicates the oxidation of $Li_2S/Li_2S_2$ to intermediate polysulfides. However, at deeper charging conditions, as shown in Figure S10d, smaller particles completely disappeared, and some of the residual $Li_2S$ particle's height increased, which is similar to the trend observed under potentiostatic conditions. However, morphological changes are subject to change with many factors including cathode surfaces and electrolyte additives, the studies of which are underway.

In summary, for the first time, in situ AFM-SECM demonstrated the nanoscale level probing of the Li−S cathode surface. A competitive SECM mode of imaging was proposed and validated to study the electrochemical aspects of LiPS redox reactions. AFM−SECM multidimensional imaging on the $Li_2S/Li_2S_2$ particle unveiled the existence of both electrochemically active (conducting) and inactive (insulating) regions and monitored their contribution toward the overall electrochemical activity during the oxidation process. The results revealed that the conducting phase of solids becomes reversible and undergoes further conversion reactions. More importantly, the insulating part, predominantly $Li_2S$, is apparently irreversible and tends to react with as-formed intermediate LiPS. Further, the LiPS species undergo subsequent reactions over charging conditions, which leads to eventual deposition of more insulating products as evidenced from in situ AFM studies. Formation of such products (mostly sulfur) on $Li_2S$ particles not only restricts further oxidation of $Li_2S$ particles but also limits the reduction of sulfur in subsequent cycles, which restricts the active materials utilization. It is anticipated that this work opens new avenues to understand the morphological and structural changes associated with the Li−S charging mechanism on the cathode surface.

DOI: 10.1021/acs.nanolett.9b01636
Nano Lett. 2019, 19, 5229−5236

## ■ ASSOCIATED CONTENT

### Supporting Information

The Supporting Information is available free of charge on the ACS Publications website at DOI: 10.1021/acs.nanolett.9b01636.

> Experimental section, in situ AFM−SECM electrochemical cell assembly, SECM approach curve fitting with the theoretical equation, cyclic voltammetry of LiPS on carbon substrate and SECM tip, Raman results, AFM images of $Li_2S$ deposition at different potentials, $Li_2S$ particle volume changes at different potentials (PDF)

## ■ AUTHOR INFORMATION

### Corresponding Author

*E-mail: leela.arava@wayne.edu.

### ORCID

Kiran Mahankali: 0000-0003-3540-5350
Naresh Kumar Thangavel: 0000-0002-6604-0211
Leela Mohana Reddy Arava: 0000-0001-6685-6061

### Author Contributions

N.K.T. and L.M.R.A. created the ideas and plan for the experiments. K.M. designed the experimental setup and carried out the experiments. N.K.T. and K.M. performed the theoretical approach curve fittings. All the authors contributed to writing this manuscript.

### Notes

The authors declare no competing financial interest.

## ■ ACKNOWLEDGMENTS

This material is based upon work supported by the National Science Foundation under Grant No. 1751472. The authors would like to thank Mr. Uday Praveen Tiruvalluri for designing the SECM electrochemical cell. N.K.T. would like to thank Dr. K.L.N. Phani, CSIR-Emeritus Scientist, IICT-Hyderabad, India, who provided constant motivation and helpful discussions during the course of these studies.

## ■ REFERENCES

(1) Xu, R.; Belharouak, I.; Zhang, X.; Chamoun, R.; Yu, C.; Ren, Y.; Nie, A.; Shahbazian-Yassar, R.; Lu, J.; Li, J. C.; et al. *ACS Appl. Mater. Interface.* **2014**, *6*, 21938−21945.

(2) Xu, R.; Lu, J.; Amine, K. *Adv. Energy. Mater.* **2015**, *5*, 1500408−1500430.

(3) Manthiram, A.; Fu, Y.; Chung, S. H.; Zu, C.; Su, Y. S. *Chem. Rev.* **2014**, *114*, 11751−87.

(4) Mikhaylik, Y. V.; Akridge, J. R. *J. Electrochem. Soc.* **2004**, *151*, A1969−A1976.

(5) Aurbach, D.; Pollak, E.; Elazari, R.; Salitra, G.; Kelley, C. S.; Affinito, J. *J. Electrochem. Soc.* **2009**, *156*, A694−A702.

(6) Yamin, H.; Gorenshtein, A.; Penciner, J.; Sternberg, Y.; Peled, E. *J. Electrochem. Soc.* **1988**, *135*, 1045−1048.

(7) Babu, G.; Masurkar, N.; Al Salem, H.; Arava, L. M. *J. Am. Chem. Soc.* **2017**, *139*, 171−178.

(8) Yuan, Z.; Peng, H. J.; Hou, T. Z.; Huang, J. Q.; Chen, C. M.; Wang, D. W.; Cheng, X. B.; Wei, F.; Zhang, Q. *Nano Lett.* **2016**, *16*, 519−527.

(9) Al Salem, H.; Babu, G.; Rao, C. V.; Arava, L. M. *J. Am. Chem. Soc.* **2015**, *137*, 11542−11545.

(10) Yan, J.; Liu, X.; Li, B. *Adv. Sci.* **2016**, *3*, 1600101−1600111.

(11) Deng, Z.; Zhang, Z.; Lai, Y.; Liu, J.; Li, J.; Liu, Y. *J. Electrochem. Soc.* **2013**, *160*, A553−A558.

(12) Diao, Y.; Xie, K.; Xiong, S.; Hong, X. *J. Electrochem. Soc.* **2012**, *159*, A1816−A1821.

(13) Jin, Y.; Zhou, G.; Shi, F.; Zhuo, D.; Zhao, J.; Liu, K.; Liu, Y.; Zu, C.; Chen, W.; Zhang, R.; et al. *Nat. Commun.* **2017**, *8*, 462−471.

(14) Zhou, G.; Sun, J.; Jin, Y.; Chen, W.; Zu, C.; Zhang, R.; Qiu, Y.; Zhao, J.; Zhuo, D.; Liu, Y.; et al. *Adv. Mater.* **2017**, *29*, 1603366.

(15) Yuan, H.; Zhang, W.; Wang, J. G.; Zhou, G.; Zhuang, Z.; Luo, J.; Huang, H.; Gan, Y.; Liang, C.; Xia, Y.; et al. *Energy. Storage. Mater.* **2018**, *10*, 1−9.

(16) Wu, H. L.; Huff, L. A.; Gewirth, A. A. *ACS Appl. Mater. Interfaces* **2015**, *7*, 1709−19.

(17) Barchasz, C.; Molton, F.; Duboc, C.; Lepretre, J. C.; Patoux, S.; Alloin, F. *Anal. Chem.* **2012**, *84*, 3973−80.

(18) Zhang, G.; Zhang, Z. W.; Peng, H. J.; Huang, J. Q.; Zhang, Q. *Small* **2017**, *1*, 1700134−1700166.

(19) Liu, N.; Zhou, G.; Yang, A.; Yu, X.; Shi, F.; Sun, J.; Zhang, J.; Liu, B.; Wu, C. L.; Tao, X.; et al. *Proc. Natl. Acad. Sci. U. S. A.* **2019**, *116*, 765−770.

(20) Ji, X.; Nazar, L. F. *J. Mater. Chem.* **2010**, *20*, 9821−9826.

(21) Manthiram, A.; Fu, Y.; Chung, S. H.; Zu, C.; Su, Y. S. *Chem. Rev.* **2014**, *114*, 11751−11787.

(22) Waluś, S.; Barchasz, C.; Colin, J. F.; Martin, J. F.; Elkaïm, E.; Leprêtre, J. C.; Alloin, F. *Chem. Commun.* **2013**, *49*, 7899−7901.

(23) Sun, Y.; Seh, Z. W.; Li, W.; Yao, H.; Zheng, G.; Cui, Y. *Nano Energy* **2015**, *11*, 579−586.

(24) Nelson, J.; Misra, S.; Yang, Y.; Jackson, A.; Liu, Y.; Wang, H.; Dai, H.; Andrews, J. C.; Cui, Y.; Toney, M. F. *J. Am. Chem. Soc.* **2012**, *134*, 6337−6343.

(25) Lang, S. Y.; Shi, Y.; Guo, Y. G.; Wang, D.; Wen, R.; Wan, L. J. *Angew. Chem., Int. Ed.* **2016**, *55*, 15835−15839.

(26) Yu, X.; Pan, H.; Zhou, Y.; Northrup, P.; Xiao, J.; Bak, S.; Liu, M.; Nam, K. W.; Qu, D.; Liu, J.; Wu, T.; Yang, X. Q. *Adv. Energy. Mater.* **2015**, *5*, 1500072.

(27) Fernández, J. L.; Wijesinghe, M.; Zoski, C. G. *Anal. Chem.* **2015**, *87*, 1066−1074.

(28) Polcari, D.; Dauphin-Ducharme, P.; Mauzeroll, J. *Chem. Rev.* **2016**, *116*, 13234−13278.

(29) Xu, F.; Beak, B.; Jung, C. *J. Solid State Electrochem.* **2012**, *16*, 305−311.

(30) Takahashi, Y.; Kumatani, A.; Munakata, H.; Inomata, H.; Ito, K.; Ino, K.; Shiku, H.; Unwin, P. R.; Korchev, Y. E.; Kanamura, K.; et al. *Nat. Commun.* **2014**, *5*, 5450.

(31) Zampardi, G.; Ventosa, E.; La Mantia, F.; Schuhmann, W. *Chem. Commun.* **2013**, *49*, 9347−9349.

(32) Bertoncello, P. *Energy Environ. Sci.* **2010**, *3*, 1620−1633.

(33) Eckhard, K.; Chen, X.; Turcu, F.; Schuhmann, W. *Phys. Chem. Chem. Phys.* **2006**, *8*, 5359−5365.

(34) Nebel, M.; Erichsen, T.; Schuhmann, W. *Beilstein J. Nanotechnol.* **2014**, *5*, 141−151.

(35) Nebel, M.; Grützke, S.; Diab, N.; Schulte, A.; Schuhmann, W. *Angew. Chem., Int. Ed.* **2013**, *52*, 6335−6338.

(36) Talaie, E.; Bonnick, P.; Sun, X.; Pang, Q.; Liang, X.; Nazar, L. F. *Chem. Mater.* **2017**, *29*, 90−105.

(37) Huang, X.; Wang, Z.; Knibbe, R.; Luo, B.; Ahad, S. A.; Sun, D.; Wang, L. *Energy. Technol.* **2019**; Early view.

(38) Zheng, D.; Zhang, X.; Wang, J.; Qu, D.; Yang, X.; Qu, D. *J. Power Sources* **2016**, *301*, 312−316.

(39) Hassoun, J.; Agostini, M.; Latini, A.; Panero, S.; Sun, Y. K.; Scrosati, B. *J. Electrochem. Soc.* **2012**, *159*, A390−A395.

(40) Cuisinier, M.; Cabelguen, P. E.; Evers, S.; He, G.; Kolbeck, M.; Garsuch, A.; Bolin, T.; Balasubramanian, M.; Nazar, L. F. *J. Phys. Chem. Lett.* **2013**, *4*, 3227−3232.

(41) Gorlin, Y.; Patel, M. U.; Freiberg, A.; He, Q.; Piana, M.; Tromp, M.; Gasteiger, H. A. *J. Electrochem. Soc.* **2016**, *163*, A930−A939.

(42) Fan, F. Y.; Carter, W. C.; Chiang, Y. M. *Adv. Mater.* **2015**, *27*, 5203−5209.

(43) Lazenby, R. A.; McKelvey, K.; Unwin, P. R. *Anal. Chem.* **2013**, *85*, 2937−2944.

(44) Feng, Z.; Kim, C.; Vijh, A.; Armand, M.; Bevan, K. H.; Zaghib, K. *J. Power Sources* **2014**, *272*, 518−521.

(45) Liu, Z.; Balbuena, P. B.; Mukherjee, P. P. *J. Phys. Chem. Lett.* **2017**, *8*, 1324−1330.
(46) Yang, G.; Shi, S.; Yang, J.; Ma, Y. *J. Mater. Chem. A* **2015**, *3*, 8865−8869.
(47) Demir-Cakan, R.; Morcrette, M.; Gangulibabu; Gueguen, A.; Dedryvere, R.; Tarascon, J. M. *Energy. Environmental. Sci.* **2012**, *6*, 176−182.
(48) Helen, M.; Reddy, M. A.; Diemant, T.; Golla-Schindler, U.; Behm, R. J.; Kaiser, U.; Fichtner, M. *Sci. Rep.* **2015**, *5*, 12146.
(49) Liu, Z.; Hubble, D.; Balbuena, P. B.; Mukherjee, P. P. *Phys. Chem. Chem. Phys.* **2015**, *17*, 9032−9039.
(50) Sun, Y. M.; Seh, Z. W.; Li, W. Y.; Yao, H. B.; Zheng, G. Y.; Cui, Y. *Nano Energy* **2015**, *11*, 579−586.
(51) Hagen, M.; Schiffels, P.; Hammer, M.; Dörfler, S.; Tübke, J.; Hoffmann, M. J.; Althues, H.; Kaskel, S. *J. Electrochem. Soc.* **2013**, *160*, A1205−A1214.
(52) Zhu, W.; Paolella, A.; Kim, C. S.; Liu, D.; Feng, Z.; Gagnon, C.; Trottier, J.; Vijh, A.; Guerfi, A.; Mauger, A.; Julien, C. M.; Armand, M.; Zaghib, K. *Sustainable. Energy. Fuels* **2017**, *1*, 737−747.
(53) Hagen, M.; Schiffels, P.; Hammer, M.; Dörfler, S.; Tübke, J.; Hoffmann, M.; Althues, H.; Kaskel, S. *J. Electrochem. Soc.* **2013**, *160*, A1205−A1214.

DOI: 10.1021/acs.nanolett.9b01636
*Nano Lett.* 2019, 19, 5229−5236